Gravity-wave induced anomalous potential vorticity gradient generating planetary waves in the winter mesosphere

Kaoru Sato[†] and Masahiro Nomoto

Department of Earth and Planetary Science, The University of Tokyo, Japan

J. Atmos. Sci., accepted.
5 June 2015

† K. Sato, Department of Earth and Planetary Science, The University of Tokyo, Hongo 7-3-1, Bunkyoku, Tokyo 113-0033, Japan (kaoru@eps.s.u-tokyo.ac.jp)

Abstract

We show that gravity wave forcing (GWF) plays a crucial role in the barotropic/baroclinic instability that is frequently observed in the mesosphere and considered an origin of planetary waves (PWs) such as quasi-two-day waves and four-day waves. Simulation data from a GW-resolving general circulation model were analyzed, focusing on the winter northern hemisphere where PWs are active. The unstable field is characterized by a significant potential vorticity (PV) maximum with an anomalous latitudinal gradient at higher latitudes that suddenly appears in mid-latitudes of the upper mesosphere. This PV maximum is attributed to an enhanced static stability (N^2) that develops through the following two processes: (1) strong PWs from the troposphere break in the middle stratosphere, causing a poleward and downward shift of the westerly jet to higher latitudes; and (2) strong GWF located above the jet simultaneously shifts and forms an upwelling in the mid-latitudes causing a significant increase in N^2. An interesting feature is that the PV maximum is not zonally uniform, but is observed only at longitudes with strong GWF. This longitudinally dependent GWF can be explained by selective filtering in the stratospheric mean flow modified by strong PWs. In the upper mesosphere, the Eliassen–Palm flux divergence by PWs has a characteristic structure, which is positive poleward and negative equatorward of the enhanced PV maximum. This is attributable to eastward and westward propagating PWs, respectively. This fact suggests that the barotropic/baroclinic instability is eliminated by simultaneous generation of eastward and westward PWs causing PV flux divergence.

1. Introduction

In both winter and summer seasons, the mesospheric dynamical field frequently satisfies a necessary condition for the barotropic and/or baroclinic (BT/BC) instability in which the potential vorticity (PV) has anomalous latitudinal gradients. In the summer hemisphere, the BT/BC instability is a likely origin of frequently observed quasi-two-day waves in that region (e.g., Plumb 1983; Randel 1994; Norton and Thuburn 1996; Fritts et al. 1999; Baumgaertner et al. 2008). In the winter hemisphere, it is a possible origin of so-called four-day waves (Randel and Lait 1991; Manney and Randel 1993; Lu et al. 2013) and is related to synoptic-scale front-like temperature disturbances (Thayer et al. 2010; Geer et al. 2013). Earlier studies examined this BT/BC instability as jet instability (e.g., Charney and Stern 1962) without describing its specific causes. Differential radiative heating may be a candidate. Several subsequent studies discussed that another possible cause of the instability is planetary wave (PW) forcing (PWF) (e.g., Baldwin and Holton 1988; Geer et al. 2013). More recently, the role of gravity wave (GW) forcing (GWF)[‡] in the formation of the unstable condition is also focused on (e.g., McLandress and McFarlane, 1993; Norton and Thuburn 1996; Watanabe et al. 2009; Ern et al. 2011).

It is well known that GWF in the upper mesosphere is important as a driving force of the residual mean circulation from the summer hemisphere to the winter hemisphere (e.g., Holton 1983; Plumb 2002). The GWF in the upper mesosphere can be modulated by PWs in the stratosphere, because GWs are filtered in stratospheric winds that are modified by the PWs (e.g., Holton 1984, Meyer et al. 1999; Smith 2003; Lieberman et al.

[‡] Forcing due to the divergence of momentum flux associated with GWs is frequently called GW drag. However, GW forcing can both accelerate and decelerate the mean flow. Thus, this paper uses “forcing” for GW forcing regardless of its sign.

2013). This means that anomalous PV fields in the mesosphere may have characteristic longitudinal structures modified by GWF.

The purpose of this study is to elucidate the three-dimensional (3D) structure and formation mechanism of BT/BC unstable fields in the winter mesosphere of the northern hemisphere (NH) where PW activity is strong in the stratosphere, and to examine PWs generated from these unstable fields in the mesosphere. We used simulation data from a GW-resolving general circulation model (GCM) reaching from the surface to the upper mesosphere (Watanabe et al. 2008). This GCM does not include GW parameterizations. Thus, all waves, including GWs, were spontaneously generated in the model, although the model is able to simulate only a limited spectral range of GWs because of its insufficient horizontal resolution. In addition, the simulated zonal mean zonal wind and temperature fields in the meridional cross section are realistic. Thus, it is expected that the momentum budget be close to that of the real atmosphere. By using this GCM simulation data, we can examine the roles of GWs and PWs separately, including the interaction among GWs, PWs, and the zonal mean flow. For example, Tomikawa et al. (2012) examined the interplay of GWs and PWs for a model-simulated sudden stratospheric warming event with an elevated stratopause similar to the real atmosphere (e.g., Siskind et al. 2007; Manney et al. 2008; Chandran et al. 2013; Hitchcock et al. 2013; Zülicke and Becker 2013). Such a momentum budget analysis for a model atmosphere provides useful information for understanding the dynamics of the real atmosphere (Limpasuvan et al. 2012).

Moreover, we applied recently derived theoretical formulas for 3D residual mean flow that are applicable to both GWs and PWs (Kinoshita and Sato 2013) to examine the 3D structure and formation mechanism of the unstable field. Hereafter this 3D theory is referred to as the 3D transformed Eulerian-mean (TEM) theory because this theory can be regarded as an extension of a commonly-used two dimensional (2D) TEM theory (e.g., Andrews et al., 1997). The 3D TEM formulas were originally derived for perturbations from the time mean, but the contribution of stationary waves can be evaluated as well using an extended Hilbert transform (Sato et al. 2013). With this method, the longitudinal structure of the unstable fields was examined.

Prior to this study, Watanabe et al. (2009) examined four-day waves in the winter mesosphere of the southern hemisphere (SH) using the same model simulation data. Through a 2D analysis of the zonal mean fields using the 2D TEM equations, it was shown that anomalous PV gradients were continuously observed in the mesosphere and the importance of GWF for maintaining the unstable fields was discussed. The difference of the present study from Watanabe et al. (2009) is that we focused on the NH winter where PW activity is stronger in the stratosphere than in the SH and analyzed 3D fields as well as zonal mean 2D fields.

The remainder of this paper is organized as follows. A brief description of the model data is given in Section 2 and a method of analysis including 3D diagnostics is described in Section 3. Section 4 presents characteristics of the BT/BC unstable fields. In Section 5, the interplay of PWs in the stratosphere and GWs that leads to the formation of the unstable fields is examined using 2D TEM analysis. In addition, a 3D analysis was performed to study the 3D structures of the unstable field. In Section 6, characteristics of PWs observed in the mesosphere with anomalous PV fields are described, and their implication is discussed. Section 7 presents summary and concluding remarks.

2. Description of model data

We used data obtained from a GW-resolving middle atmosphere GCM that had been developed for the KANTO project (Watanabe et al. 2008). This GCM is a spectral model with T213 truncation and 256 vertical levels from the ground up to an altitude of 85 km. The minimum resolvable horizontal wavelength is about 180 km and the vertical spacing is taken at 300 m from the upper troposphere up to the upper mesosphere. The GCM was integrated over three model years from initial conditions after a high level of spin-up with climatology of sea surface temperatures and an ozone layer including their seasonal variations. A sponge layer was implemented for the top six levels above 0.01 hPa corresponding to an altitude of about 80 km in the GCM. In the present study, only results for pressure levels below 0.01 hPa are shown to avoid the effect of the sponge layer. Hourly-mean meteorological fields are output every one hour. Details of the experimental setup of the GCM were described by Watanabe et al. (2008).

No GW parameterization is adopted in the model. All waves including PWs and GWs are spontaneously generated in the GCM, although only a limited spectral range of GWs was resolvable. Major sources of GWs were considered topography, jet-front systems, and convection (Watanabe et al. 2008; Sato et al. 2009, 2012). Nonetheless, the model successfully reproduced overall characteristics in seasonal variations of the middle atmosphere (Watanabe et al. 2008) and of momentum fluxes associated with GWs (Sato et al. 2009), equatorial quasi-biennial-like oscillation (e.g., Kawatani et al. 2010), semiannual oscillation (Tomikawa et al. 2010), a sudden stratospheric warming (Tomikawa et al. 2012), mesospheric four-day waves (Watanabe et al. 2009), and a fine vertical structure at the extratropical tropopause (e.g., Miyazaki et al. 2010). Large-scale GWs had realistic phase structure and amplitudes (Kawatani et al 2010, Sato et al. 2012). In addition, Geller et al. (2013) showed that the geographical distribution of GW absolute momentum flux of the KANTO model is similar to recent high-resolution satellite observations unlike global models using parameterized GWs which have anomalously high momentum fluxes at polar regions. From these previous studies, it can be expected that the momentum budgets in the meteorological fields of this model be close to the real atmosphere, including interactions among GWs, PWs, and the mean flow. Therefore, we used the model data as a surrogate for the real atmosphere.

3. Methods of analysis

a. Lait's modified potential vorticity

A necessary condition of the BT/BC instability is the existence of negative latitudinal gradients of zonal mean quasi-geostrophic potential vorticity in the atmosphere with the background static stability varying only in the vertical (e.g., Andrews et al., 1997). For an atmosphere with static stability depending on the latitude, we can use an alternate necessary condition, which is the existence of negative latitudinal gradients of zonal mean Ertel's potential vorticity (EPV) on an isentropic surface. We used the modified potential vorticity (MPV) for the analysis, which is defined as the EPV weighted by $\theta^{-\frac{9}{2}}$ (Lait 1993):

$$MPV \equiv EPV \times \left(\frac{\theta}{\theta_0}\right)^{-\frac{9}{2}} = -g\frac{f+\zeta}{\frac{\partial p}{\partial \theta}\cdot\left(\frac{\theta}{\theta_0}\right)^{\frac{9}{2}}} \propto (f+\zeta)N^2 \quad (1)$$

where θ is the potential temperature, θ_0 is its reference, ζ is the relative vorticity, f is the inertial frequency, p is the pressure, g is the magnitude of gravitational acceleration, $N^2\left(\equiv \frac{g}{\theta_0}\frac{\partial \theta}{\partial z}\right)$ is the Brunt–Väisälä frequency squared, and z is a log-pressure height. The MPV is conservative on an isentropic surface like EPV when nonconservative processes such as friction and diabatic heating are absent. Yet, unlike EPV, the MPV exhibits small vertical dependence and hence the vertical structure of its latitudinal gradient is easy to capture. The necessary condition for the BT/BC instability is the existence of a negative latitudinal gradient of zonal mean MPV on an isentropic surface:

$$\left.\frac{\partial \overline{MPV}}{\partial y}\right|_{\theta} < 0 \tag{2}$$

where y is the latitude.

In addition, as shown in (1), the MPV is roughly proportional to the product of absolute vorticity $(f + \zeta)$ and Brunt–Väisälä frequency squared (N^2). We will examine which process is more important for the formation of the anomalous potential vorticity gradient.

b. 2D TEM diagnostics

The TEM zonal momentum equation for the log-pressure coordinate is written as follows:

$$\overline{u}_t + \overline{v}^*\left[(a\cos\varphi)^{-1}(\overline{u}\cos\varphi)_\varphi - f\right] + \overline{w}^*\overline{u}_z = (\rho_0 a\cos\varphi)^{-1}\nabla\cdot\mathbf{F} + \overline{X} \tag{3}$$

$$\mathbf{F} \equiv \rho_0 a\cos\varphi\left(0, \overline{u}_z\frac{\overline{v'\theta'}}{\overline{\theta}_z} - \overline{u'v'}, \left[f - (a\cos\varphi)^{-1}(\overline{u}\cos\varphi)_\varphi\right]\frac{\overline{v'\theta'}}{\overline{\theta}_z} - \overline{u'w'}\right) \tag{4}$$

where overbars represent the zonal mean and primes represent the deviation from the zonal mean, $\overline{u}$ is the zonal mean zonal wind, $\overline{v}^*$ and $\overline{w}^*$ are the meridional and vertical components of the residual mean flow, respectively, $\mathbf{F}$ is the Eliassen–Palm (E–P) flux (e.g., Andrews et al. 1987). The term $\overline{X}$ includes horizontal and vertical diffusion and truncation errors in the model. The rest of the notations follow the convention. The wave forcing to the zonal mean zonal flow is expressed as E–P flux divergence (i.e., $\mathrm{EPFD} \equiv (\rho_0 a \cos\varphi)^{-1} \nabla \cdot \mathbf{F}$).

In order to evaluate the contribution to the wave forcing (EPFD) and the residual mean flow by respective waves, the perturbation fields are divided into two components, namely those with zonal wavenumbers s of 1 to 3 ($\mathrm{s} = 1 - 3$) as PWs and those with $\mathrm{s} > 3$ as GWs. This definition of GWs is quite rough because the $\mathrm{s} > 3$ components include synoptic-scale waves as well. However, we mainly examine GWs in terms of the wave forcing in the present paper. It was confirmed that contribution of the $\mathrm{n} > 21$ components, where n is the total wavenumber and $\mathrm{n} = 21$ roughly corresponds to a horizontal wavelength of 1800 km, that were designated as GW components by previous studies using the same model simulation data (Sato et al. 2009; Tomikawa et al. 2012; Sato et al. 2012), is quite dominant to the EPFD due to the GWs ($\mathrm{s} > 3$) (not shown in detail). Hence we took this wavenumber range ($\mathrm{s} > 3$) for the analysis of GWF. This categorization of PWs and GWs covers the whole wave fields and hence it is convenient for the momentum budget analysis as is made in later sections. In the following, PWF and GWF denote the EPFD due to the PWs ($\mathrm{s} = 1 - 3$) and that due to GWs ($\mathrm{s} > 3$), respectively.

c. Analysis of 3D residual mean flow and 3D GWF based on the 3D TEM theory

To examine the PV longitudinal structure and its formation mechanism, we conducted a 3D analysis using the 3D TEM theory recently derived by Kinoshita and Sato (2013). The 3D distribution of the vertical component of the residual mean flow $\overline{w}^*$ is calculated using the following formula

$$\overline{w}^* = \overline{w} + \overline{w}^S = \overline{w} + \left(\frac{\overline{u'\phi'_z}}{N^2}\right)_x + \left(\frac{\overline{v'\phi'_z}}{N^2}\right)_y, \qquad (5)$$

where ϕ is the geopotential. Here, perturbation components denoted by primes are extracted as the departure from the zonal mean, $\overline{w}$ is the time mean of a vertical flow, and averaging that is needed for flux calculations, i.e., the second and third terms of the right-hand side of (5), is made using an extended Hilbert transform (Sato et al., 2013). Note that the formulas for 3D residual mean flows including (5) were originally derived for departures from the time mean under the assumption of small wave amplitudes. However, these formulas are applicable to any perturbation if it can be extracted from the original fields. Thus, we used the departure from the zonal mean as the perturbation components in the present study. The lengths of averaging using the extended Hilbert transform correspond to those of individual wave packets (i.e., envelopes). This method enabled us to analyze the 3D residual mean flow fields with respect to all wave components including both stationary and transient waves. For details, see Kinoshita and Sato (2013) and Sato et al. (2013).

Moreover, in this study, 3D GW forcing was also examined as

$$\mathrm{3DGWF} \equiv -\rho_0 \frac{\partial \rho_0 \overline{u'w'}}{\partial z}, \tag{6}$$

using the time mean for averaging because this component is dominant in GWF (Sato et al. 2013), although stricter formula was derived by Kinoshita and Sato (2013).

4. Characteristics of the anomalous potential vorticity gradient in the mesosphere

Figure 1a shows a time–latitude section of zonal mean MPV and its latitudinal gradient in NH on an isentropic surface of 4000 K (roughly corresponding to an altitude of 70 km) in November through February in the second model year. The MPV generally shows a weak maximum in the mid-latitudes, which is consistent with the climatology by

Manney and Randel (1994). An interesting feature is that the MPV maximum is significantly enhanced twice around 45°N at the beginning of January and at the beginning of February. The latitudinal gradient of MPV is largely negative to the north of the enhanced MPV maximum during the two events, suggesting that the mean fields are considerably unstable.

To examine the cause of the MPV enhancement, the time–latitude sections of zonal mean N^2 and $f+\zeta$ are shown in Figs. 1b and 1c, respectively. A significant increase in N^2 is observed during the two events. In contrast, enhancements in $f+\zeta$ are also observed but are not sufficiently strong to explain the MPV maximum in the latitude direction. Moreover, particularly for the first event, it seems that the $f+\zeta$ enhancement occurred slightly after the MPV enhancement event. These features indicate that the MPV enhancements are mainly due to a significant increase in N^2. Thus, we examined the cause of the increase in N^2. In the present study, a more detailed analysis was conducted focusing on the first MPV enhancement event by dividing it into two periods, namely, the formation period of December 25–30 (hereafter referred to as F-period) and the mature period from January 1–5 (M-period). The period of December 1–6 (N-period) was also analyzed as a normal reference period.

Figure 2 shows latitude–potential temperature sections of zonal mean MPV and MPV_y (top), $\overline{u}$ and geopotential height (middle column), and temperature $\overline{T}$ and N^2 (bottom) during the N-Period (left), F-Period (middle row), and M-Period (right). For the F-Period and M-Period, the MPV maxima around 45°N are clearly visible above 3300 K (z ~65 km) with a significant anomalous MPV gradient at higher latitudes (Figs. 2a–2c). The Brunt–Väisälä frequency squared N^2 is also enhanced above 3300 K while it is minimized around 3000 K. Such a characteristic structure for N^2 is mainly related to the appearance of a significant low-temperature region around 3500 K (z ∼68 km), slightly below the MPV maximum (Figs. 2g–2i). It can be seen that temperature increases around 60°N and 2500 K, resulting in a merging of the stratopause of mid-latitudes with that of high latitudes for the F-Period and M-Period.

The westerly (i.e., eastward) jet situated around 43°N and 3000 K during the N-Period moved poleward to about 65°N and downward to a level of ∼2500 K during the F-Period and to ∼2000 K during the M-Period (Figs. 2d–2f). Such an evolution of the westerly jet is consistent with the thermal wind balance and the above-mentioned temperature change. It is also interesting that a weak westerly jet is formed around 30°N above 3500 K equatorward of the MPV maximum during the M-Period. This is consistent with the appearance of the low-temperature region in mid-latitudes.

5. Formation mechanism of the PV maximum in the mesosphere

a. Two-dimensional TEM analysis

Next, we examined the reason why a low-temperature region is formed around 45°N and 68 km, because this is a key feature for the appearance of the MPV maximum. The most plausible mechanism is an adiabatic cooling associated with an upward residual mean flow. Figure 3a shows a time–latitude section of the residual mean vertical wind $\overline{w}^*$ and $\overline{T}$ at 68 km. Upwelling (positive $\overline{w}^*$), which is weak around 30°N during the N-Period, is strengthened, suddenly shifts poleward, and is situated around 45°N during the F-Period and M-Period. The low-temperature region exhibits a similar variation to the upwelling, supporting our inference that the formation of this low-temperature region is attributable to the adiabatic cooling associated with the upwelling.

The strong upwelling at 68 km may be explained by strong negative GWF located above the upwelling through a mechanism similar to the downward control principle (Haynes et al., 1991), though the fields are not necessarily steady in the present case. When a negative GWF is present, a westward torque is given to the zonal mean zonal flow $\overline{u}$, and causes poleward $\overline{v}^*$ to latitudes with smaller absolute angular momentum to keep the geostrophic balance in the y direction. According to the continuity equation, upward and downward $\overline{w}^*$s are formed below the negative GWF at its lower and higher latitude ends, respectively.

Figure 3b shows the time–latitude section of GWF and $\mathrm{MPV_y}$ at 70 km (~4000 K) where the MPV enhancements were observed. A strong negative GWF located at 45°–50°N during the N-Period suddenly shifts poleward and is located at around 60°N during the F-Period and M-Period, which is consistent with the behavior of $\overline{w}^*$ at 68 km. Subsequently, significant negative $\mathrm{MPV_y}$ appears around the strong negative GWF region during the F-Period and M-Period. These facts indicate that the GWF is likely responsible for the formation of unstable fields for the geostrophic motions.

Figure 3c shows the time–latitude section of PWF and $\overline{\theta}$ at 70 km. It is interesting that a positive PWF is observed in a negative (i.e., anomalous) $\mathrm{MPV_y}$ region. This is an indication for the existence of unstable planetary-scale disturbances. Another interesting feature is that the negative PWF is enhanced at the beginning of January after the GWF enhancement around 60°N. This feature is also probably related to the generation of PWs associated with the formed unstable fields, as discussed later.

Next, in order to examine the interplay of GWs and PWs in more detail, we produced Figs. 4a–4i that show latitude–height sections for E–P flux, its divergence, and

$\overline{u}$ for the N-Period (left), F-Period (middle), and M-Period (right) separately for all wave components (top), PWs (middle), and GWs (bottom). Scales (i.e., units for arrows of the same length) of the E–P flux vectors are arbitrary but the same for all wave components and PWs and 3 times smaller for GWs.

In total (i.e., for all wave components; Figs. 4a–4c), a significant negative EPFD maximum is observed above 65 km for all periods. Another negative EPFD maximum is observed around 45–60 km only for the F-Period and M-Period though it is weaker during the M-Period. This second EPFD maximum is associated with E-P fluxes originating from the lower atmosphere.

Characteristics of PW E–P flux and PWF are as follows: during the N-Period, PW activity is weak (Fig. 4d); during the F-Period, strong upward and slightly equatorward E–P fluxes from the lower atmosphere are observed, and PWF is strongly negative at 30°–60°N around 55 km (Fig. 4e). This is responsible for the second negative maximum observed for the total field (Fig. 4b). The poleward and downward shift of the westerly jet as indicated in Figs. 2d–2f is probably caused by this negative PWF. A similar, but weaker PWF can be observed for the M-Period (Fig. 4f). Another important feature is a significant positive PWF above 60 km at latitudes higher than ∼60°N during the F-Period and M-Period, which is evidence for the existence of unstable PWs. It is also worth noting that the strongly negative PWF peak equatorward of the positive PWF, as indicated in Fig. 3c, seems separated from the negative PWF maximum observed around 55 km. This feature will be discussed in a later section.

We will now describe characteristics of the GWs. During the N-period, EPFD caused by GWs (i.e., GWF) is significantly negative around 75 km, slightly above the westerly jet at 30°–70°N (Fig. 4g), which is responsible for the first negative EPFD maximum of all waves (Fig. 4a). The negative GWF shifts poleward and downward following the westerly jet shift, and is located at around 70 km during the F-Period and at around 67 km during the M-Period.

As already discussed, a strongly negative EPFD suggests the existence of strong poleward residual mean flow $\overline{v}^*$ and upward and downward motions of $\overline{w}^*$ below the meridional flow at its lower and higher latitude ends, respectively. Figures 4j–4l show latitude–height sections for $\overline{w}^*$ and $\overline{T}$ for the respective periods. A cold region is observed around 30°N at 72 km during the N-Period, which is shifted poleward and downward to ∼45°N and 68 km during the F-Period and M-Period. Upward $\overline{w}^*$ is observed in the lower part of the cold region and is located near the low-latitude end of the GWF for all periods (Figs. 4g–4i), suggesting that the cold region responsible for the MPV maximum is formed by GWF-induced upwelling.

Downward $\overline{w}^*$ observed above 55 km poleward of the GWF is responsible for the existence of the polar winter stratopause where solar radiative heating is absent. This downwelling is intensified during the F-Period and M-Period, causing adiabatic warming and making the high-latitude stratopause. In addition, significant downwelling is observed around 60°N below 60 km during the F-Period and M-period. This is likely associated with the negative PWF at 30°–60°N around 55 km (Figs. 4e and 4f). This downwelling seems to cause a merging of the low latitude and high latitude stratopause that are separated during the N-Period.

Figure 5 shows a schematic illustration of the dynamics during the N-Period and F-Period related to the MPV maximum in mid-latitudes. The PWs originating from the troposphere break around the stratopause and cause negative PWF. This PWF lets the westerly jet shift poleward and downward. The GWF located above the westerly jet also shifts poleward and downward following the jet shift. Upwelling induced by the GWF forms a cold region above and equatorward of the westerly jet, and increases N^2 and hence MPV above the cold region. This is the formation mechanism of the MPV maximum in mid-latitudes and hence the BT/BC unstable fields.

The poleward shift of GWF following the westerly jet shift is a key feature of this mechanism. This synchronized shift can be explained by a selective filtering of upward propagating GWs. For simplicity, let us assume that GW spectra are symmetric between eastward and westward phase velocity domains. In weak eastward wind latitudes, most GWs can penetrate into the upper mesosphere regardless of the sign of phase velocities, and hence net GWF by breaking of the surviving GWs in the mesosphere is weak. In contrast, in strong eastward wind latitudes, a large part of eastward GWs are filtered at their critical levels before reaching the mesosphere. Thus, net GWF in the mesosphere is mainly caused by westward GWs and is, therefore, negative. An important point is that such filtering should also depend on the longitude, because wind fields in the stratosphere are largely modified by PWs.

b. 3D TEM analysis

Next we analyzed the 3D fields using the 3D TEM equations formulated by Kinoshita and Sato (2013) and the extended Hilbert transform method proposed by Sato et al. (2013). Figure 6 shows longitude–height sections of (a) time-mean temperature $\overline{T}$ and geopotential anomaly ϕ' from the zonal mean at 60°N and (b) GWF and time-mean zonal wind $\overline{u}$ at 65°N for the F-Period. It is clear from Fig. 6a that significant longitudinal structures can be observed in $\overline{T}$ and ϕ', which is similar to the findings of the observational study by Thayer et al. (2010) using SABER and UKMO data. As expected, it can be seen in Fig. 6b that negative GWF around 70 km is strong at longitudes where $\overline{u}$ is strongly eastward in the middle and upper stratosphere. This feature is consistent with our inference of selective GW filtering. It is also an important feature in Fig. 6a that $\overline{T}$ at 60°N is low at 60–70 km in longitudes where GWF at 65°N is strong around 70 km.

To confirm this selective filtering more quantitatively, we examined the spatial correlation between GWF at 70 km in the mesosphere and $\overline{u}$ in the stratosphere and mesosphere for 15°N–90°N as a function of time and height for $\overline{u}$ (Fig. 7). All displayed correlation coefficients are statistically significant at a 95% confidence level according to the t-test. During two MPV maximum events (i.e., around January 1 and February 1), the correlation is negatively high for $\overline{u}$ at 20–60 km but low for 70 km (at the same level of GWF). This feature indicates that the horizontal structure of GWF at 70 km is affected by PWs below 60 km. It is also interesting that the correlation with $\overline{u}$ above 72 km is positive. This feature suggests that PWs above 72 km are formed by the GWF having a mirror structure of PWs in the stratosphere, as discussed by Smith (2003) and Lieberman et al. (2013).

The high spatial correlation indicates the possibility that the anomalous MPV field has characteristic horizontal structures related to GWF. To examine the details, we produced horizontal maps for various quantities, which are shown in Fig. 8. Displayed are maps, from top to bottom, of GWF at 70 km and $\overline{u}$ at 50 km, $\overline{w}^*$ at 68 km, $\overline{T}$ and ϕ' at 68 km, and MPV at 4000 K, for the N-Period (left), F-Period (middle), and M-Period (right). For the N-Period, the horizontal distributions of all quantities are roughly axisymmetric around the North Pole. In contrast, those for the F-Period and M-Period have significant longitudinal structures.

During the F-Period, MPV at 4000 K is maximized in a longitudinal sector counterclockwise from 60°W to 120°E (Fig. 8k), corresponding to a low-$\overline{T}$ region at 68 km (Fig. 8h). The low-$\overline{T}$ region at 68 km corresponds to a region with significant upwelling at 68 km (Fig. 8e). Thus, the low $\overline{T}$ is likely caused by adiabatic cooling associated with the upwelling. The upwelling region at 68 km is observed equatorward of the strongly negative GWF at 70 km. The GWF distribution at 70 km is similar to $\overline{u}$ at 50 km. These results strongly indicate that the MPV maximum is formed by GWF mirroring the PWs in the stratosphere. Similar correspondences among respective quantities can be observed for the M-Period, although not as clearly as those for the F-Period. This vagueness may be partly because dynamical processes have been progressing during the M-Period to eliminate the instability.

It is also worth noting that large MPV values as seen for the F-Period and M-Period are not observed during the N-Period. This means that the MPV maximum is not formed by a PW breaking on an isentropic surface but by breaking GWs instead.

6. Characteristics of PWs in the upper mesosphere

Finally, we examined characteristics of PWs in the upper mesosphere where an anomalous MPV gradient is observed. Figure 9 shows power spectra of meridional wind fluctuations in zonal wavenumber (s) versus frequency for 70 km at 60°N for a time period from 16 December to 15 January including both the F-Period and M-Period. Note that the displayed s range of the spectra is 1–5, while PWs were defined as $s = 1 - 3$ components. Positive (negative) s's denote eastward (westward) wave propagation. Eastward waves are dominant in a wide range of frequencies corresponding to wave periods from 0.6 d to 20 d including the 4-day period. Larger s components tend to have shorter wave periods. In addition, dominant westward waves have long wave periods (> 6 d) and a zonal wavenumber $s = 1$. The existence of such eastward and westward PWs with periods longer than a few days is a characteristic feature observed in the F-Period and M-Period. In contrast, spectral densities corresponding to diurnal and semidiurnal migrating tides, which are respectively observed at $s = -1$ and the one-day period, and $s = -2$ and the half-day period, are not largely different from those for the N-Period (not shown).

As a reminder, positive PWF and negative PWF are observed poleward and equatorward of the MPV maximum (around 45°N), respectively, in Figs. 4e and 4f. It is of interest to examine which PWs contribute more to the respective PWFs. Thus, an analysis of E–P flux and PWF by dividing the PWs ($s = 1 - 3$) into four categories according to their propagation direction (eastward or westward) and wave period [long periods (>6 d) or short periods (1.5–6 d)] was conducted.

Figure 10 shows latitude–height sections for E–P flux, PWF, and zonal mean zonal wind, from top to bottom, for long-period eastward PWs, long-period westward PWs, short-period eastward PWs, and short-period westward PWs for the F-Period (left) and M-Period (right). It is interesting that the negative and positive PWF maxima are attributable to different PWs: the positive PWF is due to eastward PWs (Figs. 10a, 10e, and 10f), while the negative PWF is due to westward PWs (Figs. 10c and 10d). The E–P flux vectors associated with the eastward PWs point downward from a positive PWF region to a negative one at high latitudes, indicating that the eastward PWs are generated by the BC instability. In contrast, E–P flux vectors associated with the westward PWs point upward and equatorward from a positive PWF region to a negative one, suggesting that the westward PWs are due to a mixture of BC and BT instabilities. Another interesting feature is the difference in the wave period of dominant eastward PWs between the F-Period and M-Period: long-period components are dominant during the F-Period, while short-period components dominate the M-Period. Contribution by short-period westward PWs is small during both the F-Period and M-Period.

The quasi-geostrophic theory indicates that a positive EPFD is equivalent to a poleward PV flux, while a negative EPFD indicates an equatorward PV flux (see Equation (3.5.10) of Andrews et al. 1987). Thus, the characteristic PWF (i.e., EPFD) structure that is positive at high latitudes and negative at low latitudes indicates the existence of a divergence of PV flux around the MPV maximum. Thus, the results shown in Fig. 10 suggest that the eastward and westward PWs share roles to eliminate the MPV maximum at higher and lower latitudes, respectively. It is also worth noting that internal Rossby waves propagating eastward relative to the mean wind can exist in a region with a negative latitudinal PV gradient. Such a negative PV gradient may explain why eastward PWs have fast phase speeds, although detailed theoretical studies are necessary.

7. Summary and concluding remarks

This study examined the formation of unstable fields with anomalous PV gradients and the generation of PWs associated with the BT/BC instability in the northern winter mesosphere where PWs are active in the middle atmosphere, utilizing simulation data from a GW-resolving GCM. It was shown that GW forcing plays a crucial role in forming an anomalous PV gradient. The unstable fields are characterized by an enhanced PV maximum in the mid-latitudes of the upper mesosphere. This PV enhancement was due mainly to a significant increase in N^2 by strong cooling below. This cooling occurred through the following mechanism.

1. Strong PWs originating from the troposphere break in the stratosphere and cause a negative E–P flux divergence.
2. This PWF makes an eastward jet located at 40°N in the upper stratosphere shift poleward and downward to 65°N in the middle stratosphere.
3. The GWF located in the mesosphere above the eastward jet also shifts poleward and downward following the jet shift, and forms strong upwelling equatorward of the eastward jet around 45°N.
4. This upwelling causes significant adiabatic cooling and forms the N^2 enhancement.

Next, horizontal structures of the PV maximum were examined using a 3D TEM theory. The PV was maximized in a particular longitude sector. According to the 3D TEM analysis, this sector corresponds to the area where GWF is maximized. Such a horizontal distribution of the mesospheric GWF accords well with the distribution of stratospheric eastward winds. This correspondence between the GWF and eastward winds can be explained by the selective filtering of GWs in the stratospheric winds. In other words, the PV maximum is caused by the GWF mirroring the PWs in the stratosphere.

Moreover, the EPFD equatorward and poleward of the PV maximum in the mesosphere was negative and positive, respectively. This fact means that the PV flux is equatorward and poleward from the PV maximum so as to make the PV peak shallower. In other words, the generation of PWs through BT/BC instability in the mesosphere is regarded as an adjustment process against an anomalous PV distribution caused by forcing due to GWs propagating from the lower atmosphere. An important fact is that the PV fluxes equatorward and poleward from the PV maximum are associated with different PWs, namely, westward waves and eastward waves. This point is one of interesting and new findings from the present study. It seems that the four-day wave observed in the winter mesosphere is one of such eastward PWs.

We suggest that this scenario can occur in the real atmosphere although it is elucidated by the simulation using a high resolution GCM, which covers only a portion of GWs. It is important to confirm the reality using observational data and reanalysis data. In addition, it seems that these processes occur at a time scale of days to a few tens of days. The transient response of the PV fields to the GWF, and the planetary (Rossby) wave adjustment against such anomalous PV fields should be examined theoretically. In particular, the relation between the PWs causing the EPFD in the stratosphere and those responsible for the EPFD in the mesosphere is interesting. The former PWs may act as a trigger to the generation or amplification of the latter ones in the BT/BC instability directly and/or indirectly through GWF.

It is also worth noting that the negative GWF in the mesosphere is partly cancelled by positive PWF poleward of the MPV maximum (Fig. 4). The generation of PWs from the instability caused by parameterized-GWF and its ability of significant compensation for the parameterized-GWF have been well-known among climate model scientists (e.g., McLandress and McFarlane, 1993). Cohen et al. (2013) indicated that this compensation leads to difficulty in evaluation of relative contribution of PWF and parameterized orographic GWF to the driving of the Brewer-Dobson circulation (BDC) in the stratosphere. Thus, commonly-made linear separation of the driving force of the BDC may mislead interpretation of relative roles of GWs and RWs. Sigmond and Shepherd (2014) carefully examined the credibility of climate model projections of the strengthened BDC by taking this effect into consideration. Nevertheless, we should emphasize the importance of improvement of the GW parameterizations, because generated PWs, which may be substantial for the momentum and/or energy budget in the mesosphere and lower thermosphere, can be regulated by the parameterized GWF in the whole atmosphere models. The wind and temperature fields in the mesosphere and lower thermosphere may modify the propagation of PWs below that originate from the troposphere, and hence the distribution of PWF in the stratosphere. Such modification may sometimes extend down to the troposphere. It is also discussed by using gravity-wave resolving models (Tomikawa et al., 2012; Zülicke and Becker, 2013) and by global models with parameterized GWF (e.g., Liu and Roble, 2002; Limpasuvan et al., 2012; Miller et al., 2013) that RWs and GWs can interplay in the stratosphere and mesosphere during sudden stratospheric warming events. The potential cancellation between RWF and GWF indicated by Cohen et al. may be different for the SSW, because of the high transiency and nonlinearity of this phenomenon, while most characteristics of the BDC can be discussed as a steady state. It is worth noting that that the interplay seems robust among these studies, although its details are different. These issues regarding the interplay of RWs and GWs are quite interesting and should be further examined observationally and theoretically. Observations using VHF Doppler radars providing GW momentum fluxes at high latitudes (e.g., Sato et al., 2014) will be useful. It is also important to elucidate the role of a full spectrum of GWs quantitatively using much higher resolution models. However, these issues are beyond the scope of the present paper and we leave these for future work.

Acknowledgments

We thank Elisa Manzini, Kota Okamoto and Yoshihiro Tomikawa for their invaluable comments. Thanks are also due to three anonymous reviewers for their constructive comments. Several figures were drawn by Akihiro Masuda. This work was supported by a Grant-in-Aid for Scientific Research (19204047) from MEXT, Japan. The model simulations were conducted using the Earth Simulator. Figures were prepared using the GFD-DENNOU library.

References

Andrews, D. G., J. R. Holton, and C. B. Leovy, 1987: *Middle atmosphere Dynamics*, 489 pp, Academic Press.

Baldwin, M. P., and J. R. Holton, 1988: Climatology of the stratospheric polar vortex and planetary wave breaking. *J. Atmos. Sci.,* **45,** 1123–1142.

Baumgaertner, A. J. G., A. J. McDonald, R. E. Hibbins, D. C. Fritts, D. J. Murphy, R. A. Vincent, 2008: Short-period planetary waves in the Antarctic middle atmosphere. *J. Atmos. Solar-Terr. Phys.,* **70,** 1336–1350.

Chandran A., R. L. Collins, R. R. Garcia, D. R. Marsh, V. L. Harvey, J. Yue, and L. de la Torre (2013), A climatology of elevated stratopause events in the whole atmosphere community climate model. *J. Geophys. Res. Atmos.,* **118,** 1234-1246, doi:10.1002/jgrd.50123.

Charney, J. G., and M. E. Stern, 1962: On the stability of internal baroclinic jets in a rotating atmosphere. *J. Atmos. Sci.,* **19,** 159–172.

Cohen, N. Y., E. P. Gerber, and O. Bühler, 2013: Compensation between Resolved and Unresolved Wave Driving in the Stratosphere: Implications for Downward Control. *J. Atmos. Sci.,* **70,** 3780–3798.

Ern, M., P. Preusse, J. C. Gille, C. L. Hepplewhite, M. G. Mlynczak, J. M. Russell III, and M. Riese, 2011: Implications for atmospheric dynamics derived from global observations of gravity wave momentum flux in stratosphere and mesosphere. *J. Geophys. Res.,* **116,** D19107, doi:10.1029/2011JD015821.

Fritts, D. C., J. R. Isler, R. S. Lieberman, M. D. Burrage, D. R. Marsh, T. Nakamura, T. Tsuda, R. A. Vincent, and I. M. Reid, 1999: Two-day wave structure and mean flow interactions observed by radar and High Resolution Doppler Imager. *J. Geophys. Res.,* **104(D4),** 3953–3969, doi:10.1029/1998JD200024.

Geller, M. A., M. J. Alexander, P. T. Love, J. Bacmeister, M. Ern, A. Hertzog, E. Manzini, P. Preusse, K. Sato, A. A. Scaife, and T. Zhou, 2013: A Comparison between Gravity Wave Momentum Fluxes in Observations and Climate Models. *J. Climate,* **26,** 6383–6405.

Greer, K., J. P. Thayer, and V. L. Harvey, 2013: A climatology of polar winter stratopause warmings and associated planetary wave breaking. *J. Geophys. Res. Atmos.,* **118,** 4168–4180, doi:10.1002/jgrd.50289.

Haynes, P. H., C. J. Marks, M. E. McIntyre, T. G. Shepherd, and K. P. Shine, 1991: On the “downward control” of extratropical diabatic circulations by eddy-induced mean zonal forces. *J. Atmos. Sci.,* **48,** 651–678.

Hitchcock, P., T. G. Shepherd, and G. L. Manney, 2013: Statistical characterization of arctic polar-night jet oscillation events. *J. Climate,* **26,** 2096–2116.

Holton, J. R., 1983: The influence of gravity wave breaking on the general circulation of the middle atmosphere. *J. Atmos. Sci.,* **40,** 2497–2507.

Holton, J. R., 1984: The generation of mesospheric planetary waves by zonally asymmetric gravity wave breaking. *J. Atmos. Sci.,* **41,** 3427–3430.

Kawatani, Y., K. Sato, T. J. Dunkerton, S. Watanabe, S. Miyahara, and M. Takahashi, 2010: The roles of equatorial trapped waves and internal inertia-gravity waves in driving the quasi-biennial oscillation. Part I: zonal mean wave forcing. *J. Atmos. Sci,* **67,** 963–980.

Kinoshita, T., and K. Sato, 2013: A formulation of three-dimensional residual mean flow applicable both to inertia-gravity waves and to Rossby waves. *J. Atmos. Sci.,* **70,** 1577–1602.

Lait, L. R., 1994: An alternative form for potential vorticity. *J. Atmos. Sci.,* **51,** 1754–1759.

Lieberman, R. S., D. M. Riggin, and D. E. Siskind, 2013: Stationary waves in the wintertime mesosphere: Evidence for gravity wave filtering by stratospheric planetary waves. *J. Geophys. Res. Atmos.,* **118,** 3139–3149, doi:10.1002/jgrd.50319.

Limpasuvan, V., J. H. Richter, Y. J. Orsolini, F. Stordal, and O.-K. Kvissel, 2012: The roles of planetary and gravity waves during a major stratospheric sudden warming as characterized in WACCM. *J. Atmos. Solar-Terr. Phys.,* **78-79,** 84–98, DOI: 10.1016/j.jastp.2011.03.004.

Liu, H.-L. and R. G. Roble, 2002: A study of a self-generated stratospheric sudden warming and its mesospheric-lower thermospheric impacts using the coupled TIME-GCM/CCM3. J. Geophys. Res. 107, 23: D4695. doi:10.1029/2001JD001533.

Lu, X., X. Chu, T. Fuller-Rowell, L. Chang, W. Fong, and Z. Yu, 2013: Eastward propagating planetary waves with periods of 1–5 days in the winter Antarctic stratosphere as revealed by MERRA and lidar. *J. Geophys. Res. Atmos.,* **118,** 9565–9578, doi:10.1002/jgrd.50717.

Manney, G. L., and W. J. Randel, 1993: Instability at the winter stratopause: A mechanism for the 4-day wave. *J. Atmos. Sci.,* **50,** 3928–3938.

Manney, G. L., et al., 2008: The evolution of the stratopause during the 2006 major warming: Satellite data and assimilated meteorological analyses. *J. Geophys. Res.,* **113,** D11115, doi:10.1029/2007JD009097.

McLandress, C., and N. A. McFarlane, 1993: Interactions between orographic gravity wave drag and forced stationary planetary waves in the winter Northern Hemisphere middle atmosphere. *J. Atmos. Sci.,* **50,** 1966–1990.

Meyer, C. K., 1999: Gravity wave interactions with mesospheric planetary waves: A mechanism for penetration into the thermosphere-ionosphere system. *J. Geophys. Res.,* **104,** 28181–28196, doi:10.1029/1999JA900346.

Miller, A., H. Schmidt & F. Bunzel, 2013: Vertical coupling of the middle atmosphere during stratospheric warming events. J. Atmos. Sol.-Terr. Phys. 97: 11 - 21. doi:10.1016/j.jastp.2013.02.008.

Miyazaki, K., S. Watanabe, Y. Kawatani, Y. Tomikawa, M. Takahashi, and K. Sato, 2010: Transport and mixing in the extratropical tropopause region in a high vertical resolution GCM. Part I: Potential vorticity and heat budget analysis. *J. Atmos. Sci.,* **67,** 1293–1314.

Norton, W. A., and J. Thuburn, 1996: The two-day wave in a middle atmosphere GCM. *Geophys. Res. Lett.,* **23,** 2113-2116.

Plumb, R. A., 1983: Baroclinic instability of the summer mesosphere: A mechanism for the quasi-two-day wave?. *J. Atmos. Sci.,* **40,** 262–270.

Plumb, R. A., 2002: Stratospheric transport. *J. Meteorol. Soc. Japan,* **80 (4B),** 793–809.

Randel, W. J., 1994: Observations of the 2-day wave in NMC stratospheric analyses. *J. Atmos. Sci.,* **51,** 306–313.

Randel, W. J., and L. R. Lait, 1991: Dynamics of the 4-day wave in the southern hemisphere polar stratosphere. *J. Atmos. Sci.*, **48,** 2496–2508.

Sato, K., S. Watanabe, Y. Kawatani, Y. Tomikawa, K. Miyazaki, and M. Takahashi, 2009: On the origins of mesospheric gravity waves. *Geophys. Res. Lett.*, **36,** L19801, doi:10.1029/2009GL039908.

Sato, K., S. Tateno S. Watanabe, and Y. Kawatani, 2012: Gravity wave characteristics in the Southern Hemisphere revealed by a high-resolution middle-atmosphere general circulation model. *J. Atmos. Sci.*, **69,** 1378–1396.

Sato, K., T. Kinoshita, and K. Okamoto, 2013: A new method to estimate three-dimensional residual mean circulation in the middle atmosphere and its application to gravity-wave resolving general circulation model data. *J. Atmos. Sci.*, **70,** 3756–3779.

Sato, K., M. Tsutsumi, T. Sato, T. Nakamura, A. Saito, Y. Tomikawa, K. Nishimura, M. Kohma, H. Yamagishi and T. Yamanouchi, 2014: Program of the Antarctic Syowa MST/IS Radar (PANSY), *J. Atmos. Solar-Terr. Phys.*, **118, Part A,** 2–15.

Sigmond, M. and T. G. Shepherd, 2014: Compensation between Resolved Wave Driving and Parameterized Orographic Gravity Wave Driving of the Brewer–Dobson Circulation and Its Response to Climate Change. *J. Climate*, **27,** 5601–5610.

Siskind, D. E., S. D. Eckermann, L. Coy, J. P. McCormack, *and* C. E. Randall, 2007: On recent interannual variability of the Arctic winter mesosphere: Implications for tracer descent, *Geophys. Res. Lett.*, **34,** L09806, doi:10.1029/2007GL029293.

Smith, A. K., 2003: The origin of stationary planetary waves in the upper mesosphere. *J. Atmos. Sci.*, **60,** 3033–3041.

Thayer, J. P., K. Greer, and V. L. Harvey, 2010: Front-like behavior in the Arctic wintertime upper stratosphere and lower mesosphere. *J. Geophys. Res.,* **115,** D00N04, doi:10.1029/2010JD014278.

Tomikawa, Y., K. Sato, S. Watanabe, Y. Kawatani, K. Miyazaki, and M. Takahashi, 2010: Wintertime temperature maximum at the subtropical stratopause in a T213L256 GCM. *J. Geophys. Res.,* **113,** D17117, doi:10.1029/2008JD009786.

Tomikawa, Y., K. Sato, S. Watanabe, Y. Kawatani, K. Miyazaki, and M. Takahashi, 2012: Growth of planetary waves and the formation of an elevated stratopause after a major stratospheric sudden warming in a T213L256 GCM. *J. Geophys. Res.,***117,** D16101, doi:10.1029/2011JD017243.

Watanabe, S., Y. Kawatani, Y. Tomikawa, K. Miyazaki, M. Takahashi, and K. Sato, 2008: General aspects of a T213L256 middle atmosphere general circulation model. *J. Geophys. Res.,* **113,** D12110, doi:10.1029/2008JD010026.

Watanabe, S., Y. Tomikawa, K. Sato, Y. Kawatani, K. Miyazaki, and M. Takahashi, 2009: Simulation of the eastward 4-day wave in the Antarctic winter mesosphere using a gravity wave resolving general circulation model. *J. Geophys. Res.,* **114,** D16111, doi:10.1029/2008JD011636.

Zülicke, C., and E. Becker, 2013: The structure of the mesosphere during sudden stratospheric warmings in a global circulation model. *J. Geophys. Res. Atmos.,* **118,** 2255–2271, doi:10.1002/jgrd.50219.

Figure captions

Figure 1. Time–latitude sections of (a) zonal mean modified potential vorticity (MPV) (colors) and its latitudinal gradient (MPV$_y$) (contours), ten times common logarithms (i.e., decibel) of (b) zonal mean Brunt–Väisälä frequency squared (N^2), and (c) absolute vorticity ($\zeta + f$) on an isentropic surface of $\theta =$4000 K (a height of about 70 km). Contour intervals are 5 × 10^{-12} K kg^{-1} m s^{-1} for (a), and 1 dB for (b) and (c). N, F, and M in the abscissa denote N-, F-, and M-Periods, respectively.

Figure 2. Latitude–potential temperature sections of: (a), (b), and (c) zonal mean modified potential vorticity (MPV) (colors) and its latitudinal gradient (MPV$_y$) (contours); (d), (e), and (f) zonal mean zonal wind ($\overline{u}$) (colors) and geopotential height (contours); (g), (h), and (i) zonal mean temperature ($\overline{T}$) (colors) and Brunt–Väisälä frequency squared (N^2) for the N-Period (a, d, g), F-Period (b, e, h), and M-Period (c, f, i). Contour intervals are 4 × 10^{-12} K kg^{-1} m s^{-1} for MPV$_y$, 5 km for geopotential height, and 1 × 10^{-4} s^{-2} for N^2.

Figure 3. Time–latitude sections of (a) residual mean vertical flow ($\overline{w}^*$) (colors) and zonal mean temperature ($\overline{T}$) (contours) at 68 km, (b) zonal mean gravity wave forcing (GWF) (colors) and latitudinal gradient of modified potential vorticity (MPV$_y$) on an isentropic surface (contours) at 70 km, and (c) zonal mean planetary wave forcing (PWF) (colors) and potential temperature ($\overline{\theta}$) (contours) at 70 km. Contour intervals are (a) 10 K, (b) 5 × 10^{-12} K kg^{-1} m s^{-1}, and (c) 250 K. N, F, and M in the abscissa denote N-, F-, and M-Periods, respectively.

Figure 4. Latitude–height sections of E–P flux (arrows), E–P flux divergence (EPFD) (colors), and zonal mean zonal wind ($\overline{u}$) (contours) for all wave components (a, b, c), planetary waves (d, e, f), (g), and gravity waves (g, h, i) for the N-Period (a, d, g), F-

Period (b, e, h), and M-Period (c, f, i). Scales (i.e., units for arrows of the same length) of the E–P flux vectors are arbitrary but the same for all wave components and planetary waves (PWs) and 3 times smaller for gravity waves (GWs). Color scales for EPFD are the same for all wave components, PWs and GWs. Contour interval of $\overline{u}$ is 20 m s^{-1}. Latitude–height sections of residual mean vertical flow ($\overline{w}^*$) (colors) and zonal mean temperature ($\overline{T}$) (contours) for the N-Period (j), F-Period (k), and M-Period (l). Contour interval for $\overline{T}$ is 10 K.

Figure 5. A schematic illustration of the formation mechanism of the anomalous potential vorticity (PV) field (i.e., a PV maximum in the upper mesosphere) for the N-Period (left) and F-Period and M-Period (right) in a latitude–height section. The letter J represents a westerly jet; PW represents planetary waves; GWF and PWF represent gravity wave forcing and planetary wave forcing, respectively; black arrows show the residual mean flows; C denotes a cold area; PV is represented by the dark gray area; thick curves show the stratopause.

Figure 6. Longitude–height sections of (a) time-mean temperature ($\overline{T}$) (colors) and geopotential anomaly (ϕ') from the zonal mean (contours) at 60°N, and (b) time-mean gravity wave forcing (3DGWF) (colors) and zonal wind ($\overline{u}$) (contours) at 65°N. Contour intervals are (a) 4×10^3 m^2 s^{-2} and (b) 20 m s^{-1}.

Figure 7. Time–height section of the spatial correlation between gravity wave forcing at 70 km and zonal wind at each level. The vertical axis shows the height of zonal wind.

Figure 8. Polar stereo projection maps of time-mean gravity wave forcing (3DGWF) at 70 km (colors) and zonal wind ($\overline{u}$) at 50 km (contours) (a, b, c), residual mean vertical flows ($\overline{w}^*$) at 68 km (colors) (d, e, f), time-mean temperature ($\overline{T}$) (colors) and geopotential

anomalies (ϕ') from the zonal mean at 68 km (contours) (g, h, i), time-mean modified potential vorticity (MPV) at 4000 K for (j, k, l), for the N-Period (a, d, g, j), F-Period (b, e, h, k), and M-Period (c, f, i, l). Contour intervals are 30 m s^{-1} (a, b, c) and 4×10^3 m^2 s^{-2} (g, h, i).

Figure 9. Frequency–zonal wavenumber power spectra of meridional wind fluctuations at 70 km and 60°N for the time period of December 16 to January 15 including F-Period and M-Period. Positive and negative zonal wavenumbers mean eastward and westward phase propagations, respectively.

Figure 10. Latitude–height sections of E–P fluxes (vectors), E–P flux divergence (colors) and zonal mean zonal wind ($\overline{u}$) (contours) for long-period eastward planetary waves with $s = 1 - 3$ (PWs) (a and b), long-period westward PWs (c and d), short-period eastward PWs (e and f), and short-period westward PWs (g and h) for the F-Period (a, c, e, g) and M-Period (b, d, f, h). Long and short periods mean the wave periods longer than 6 d and those of 0.6 d to 20 d, respectively. Color scale for the E–P flux divergence is the same as in Fig. 4. Contour interval is 20 m s^{-1}.

Figure 01
Click here to download Rendered Figure: Fig01v2.pdf

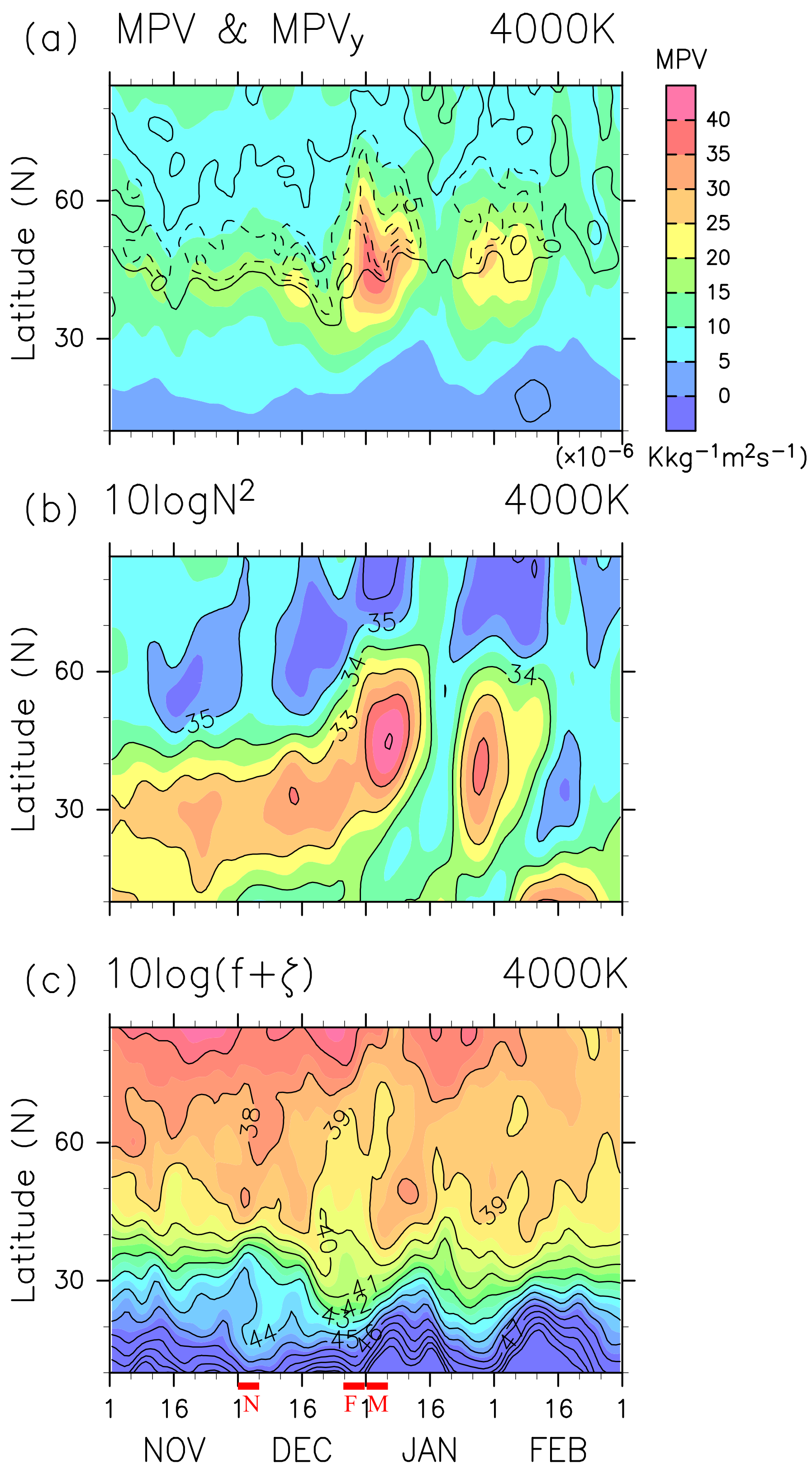

Figure 1. Time–latitude sections of (a) zonal mean modified potential vorticity (MPV) (colors) and its latitudinal gradient (MPV$_y$) (contours), ten times common logarithms (i.e., decibel) of (b) zonal mean Brunt–Väisälä frequency squared (N^2), and (c) absolute vorticity ($\zeta + f$) on an isentropic surface of θ =4000 K (a height of about 70 km). Contour intervals are 5×10^{-12} K kg^{-1} m s^{-1} for (a), and 1 dB for (b) and (c). N, F, and M in the abscissa denote N-, F-, and M-Periods, respectively.

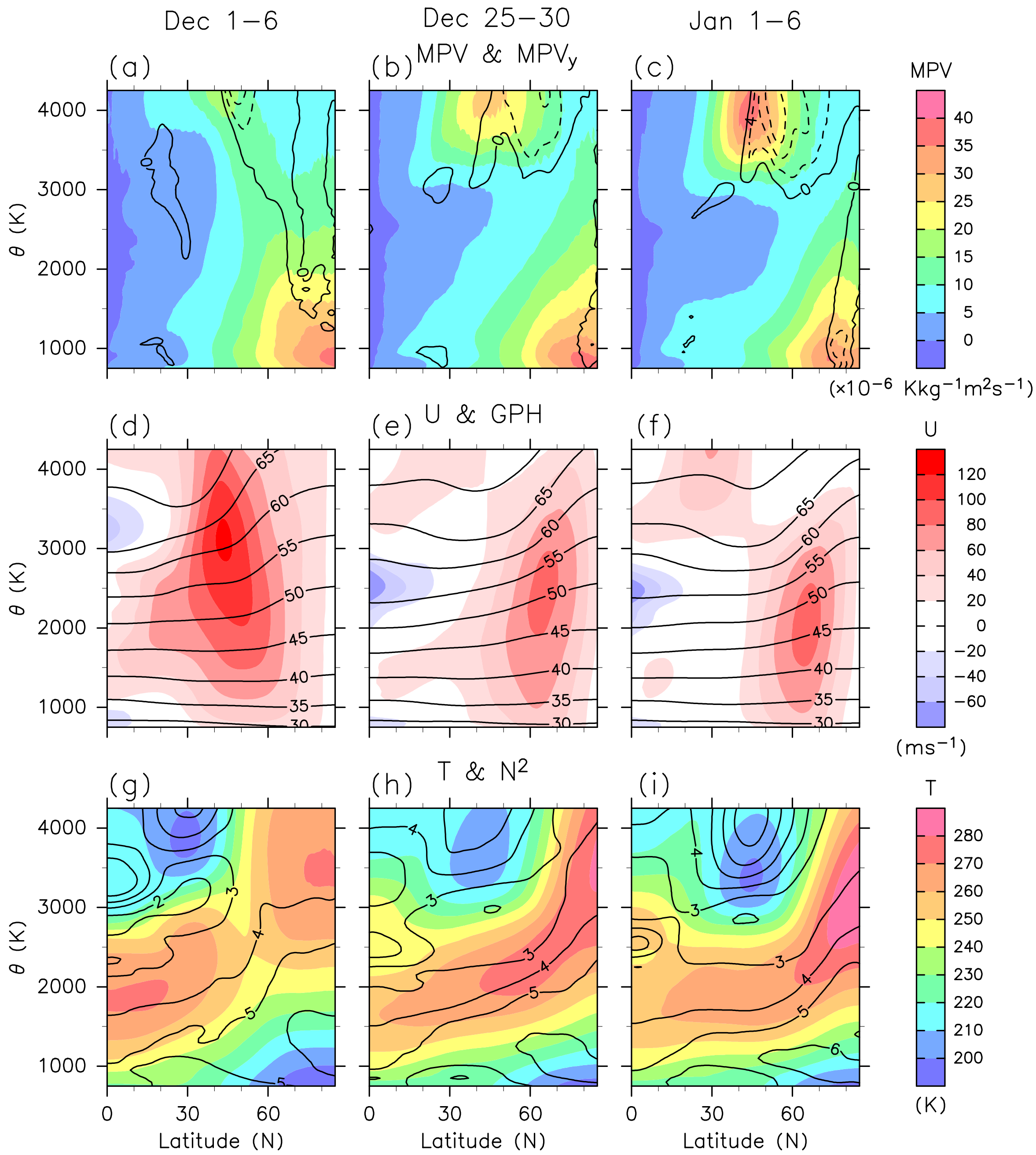

Figure 2. Latitude–potential temperature sections of: (a), (b), and (c) zonal mean modified potential vorticity (MPV) (colors) and its latitudinal gradient (MPV_y) (contours); (d), (e), and (f) zonal mean zonal wind ($\overline{u}$) (colors) and geopotential height (contours); (g), (h), and (i) zonal mean temperature ($\overline{T}$) (colors) and Brunt–Väisälä frequency squared (N^2) for the N-Period (a, d, g), F-Period (b, e, h), and M-Period (c, f, i). Contour intervals are 4×10^{-12} K kg^{-1} m s^{-1} for MPV_y, 5 km for geopotential height, and 1×10^{-4} s^{-2} for N^2.

Figure 03
Click here to download Rendered Figure: Fig03v2.pdf

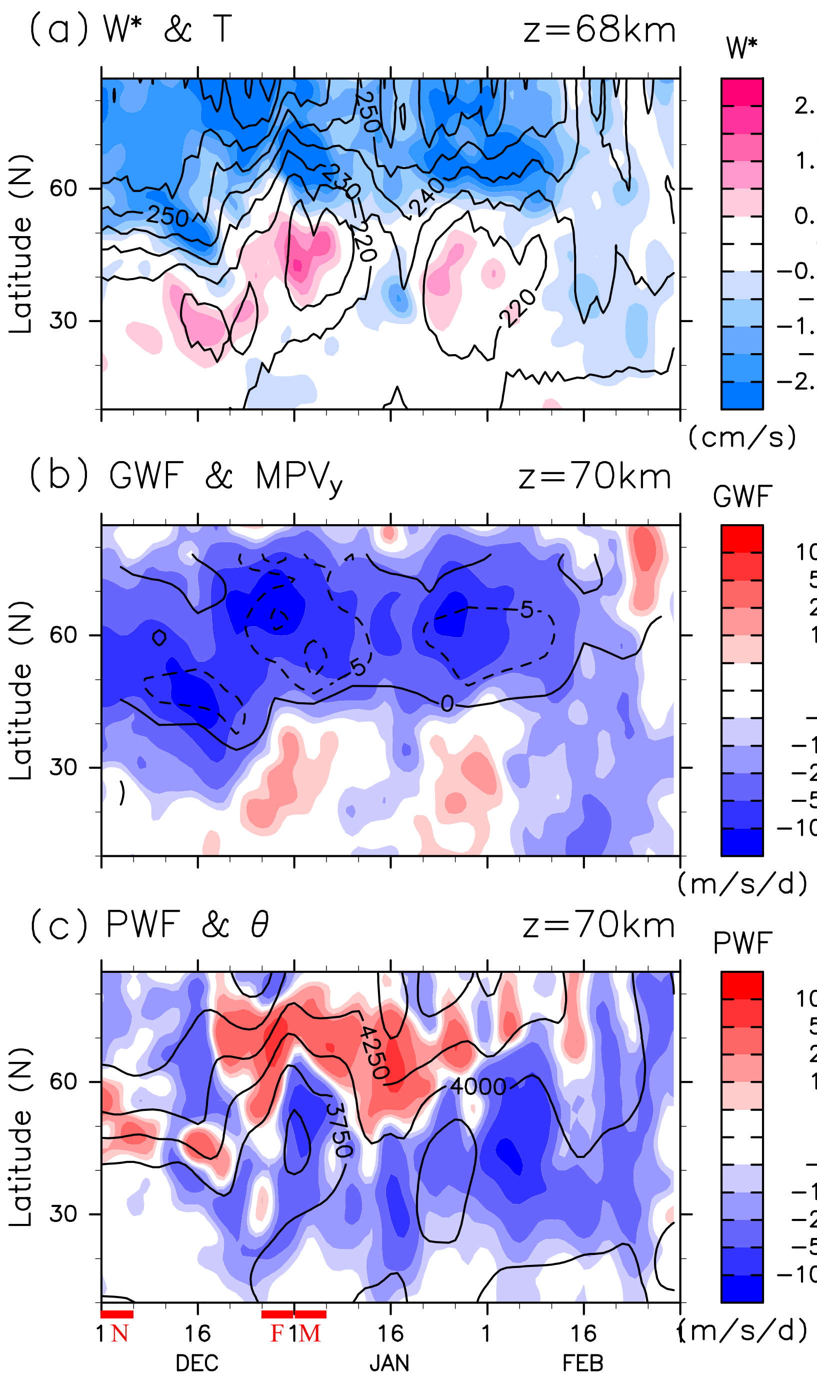

Figure 3. Time–latitude sections of (a) residual mean vertical flow ($\overline{w}^*$) (colors) and zonal mean temperature ($\overline{T}$) (contours) at 68 km, (b) zonal mean gravity wave forcing (GWF) (colors) and latitudinal gradient of modified potential vorticity (MPV_y) on an isentropic surface (contours) at 70 km, and (c) zonal mean planetary wave forcing (PWF) (colors) and potential temperature ($\overline{\theta}$) (contours) at 70 km. Contour intervals are (a) 10 K, (b) 5×10^{-12} K kg^{-1} m s^{-1}, and (c) 250 K. N, F, and M in the abscissa denote N-, F-, and M-Periods, respectively.

Figure 04

Click here to download Rendered Figure: Fig04v2.pdf

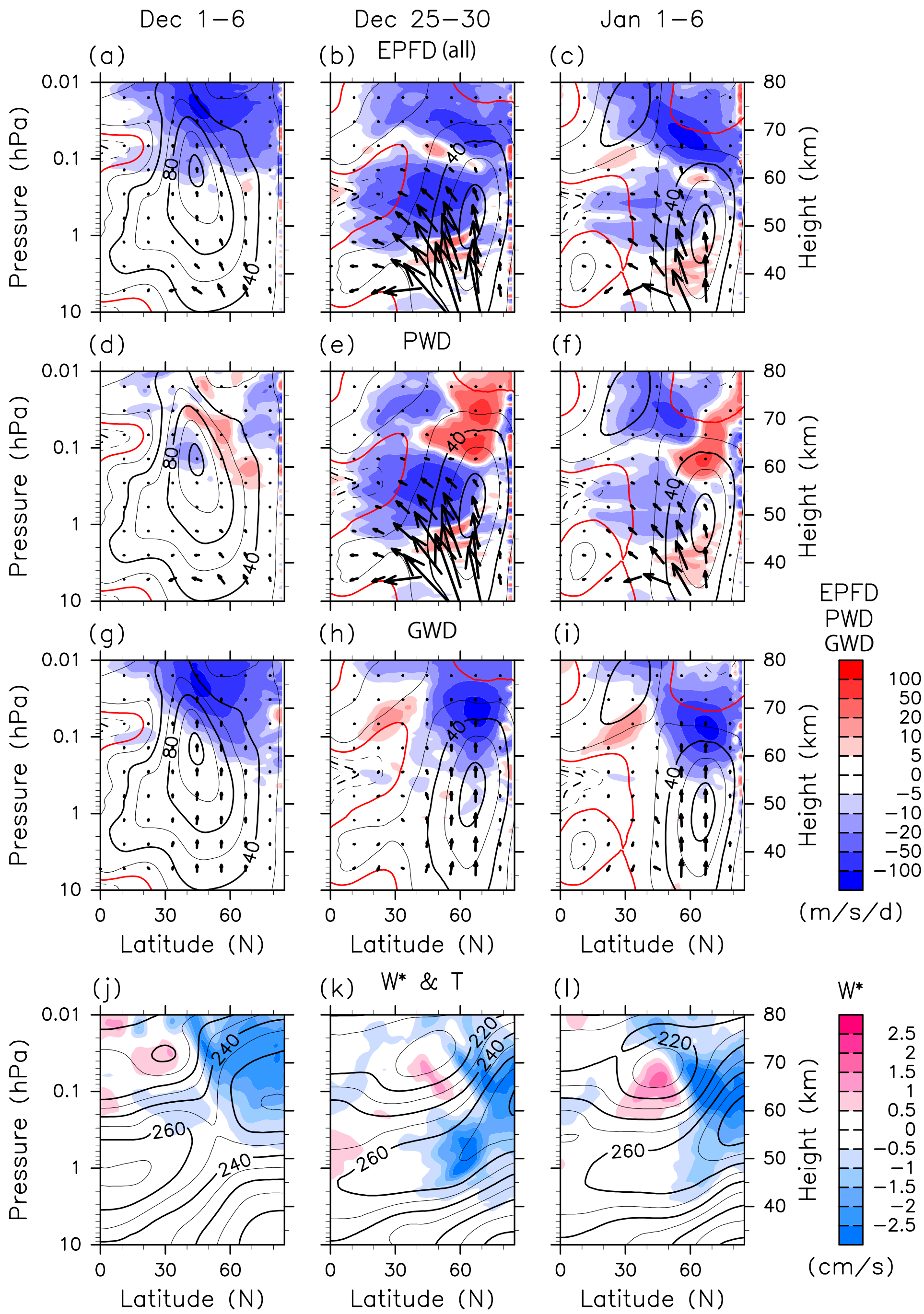

Figure 4. Latitude–height sections of E–P flux (arrows), E–P flux divergence (EPFD) (colors), and zonal mean zonal wind ($\overline{u}$) (contours) for all wave components (a, b, c), planetary waves (d, e, f), (g), and gravity waves (g, h, i) for the N-Period (a, d, g), F-Period (b, e, h), and M-Period (c, f, i). Scales (i.e., units for arrows of the same length) of the E–P flux vectors are arbitrary but the same for all wave components and planetary waves (PWs) and 3 times smaller for gravity waves (GWs). Color scales for EPFD are the same for all wave components, PWs and GWs. Contour interval of $\overline{u}$ is 20 m s^{-1}. Latitude–height sections of residual mean vertical flow ($\overline{w}^{*}$) (colors) and zonal mean temperature ($\overline{T}$) (contours) for the N-Period (j), F-Period (k), and M-Period (l). Contour interval for $\overline{T}$ is 10 K.

Figure 05

Click here to download Rendered Figure: Fig05v2.pdf

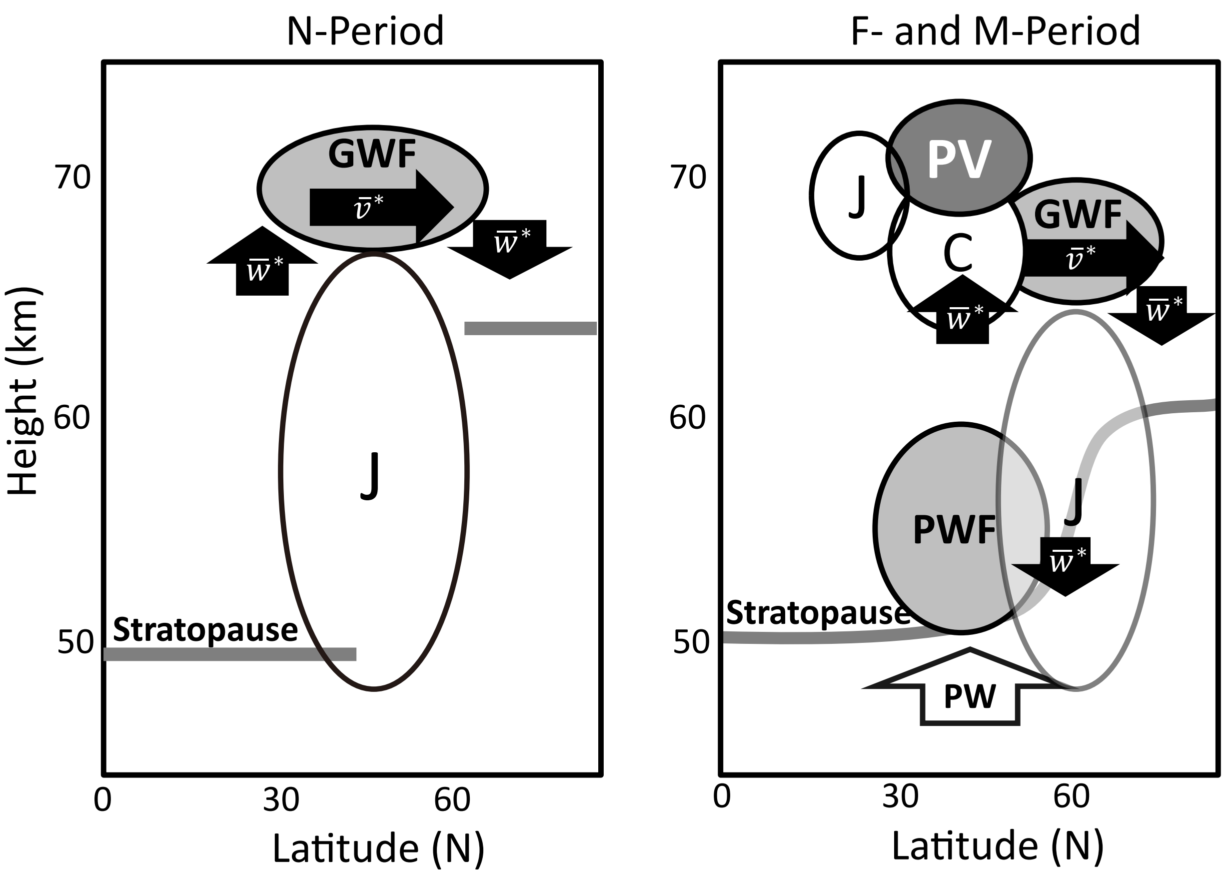

Figure 5. A schematic illustration of the formation mechanism of the anomalous potential vorticity (PV) field (i.e., a PV maximum in the upper mesosphere) for the N-Period (left) and F-Period and M-Period (right) in a latitude–height section. The letter J represents a westerly jet; PW represents planetary waves; GWF and PWF represent gravity wave forcing and planetary wave forcing, respectively; black arrows show the residual mean flows; C denotes a cold area; PV is represented by the dark gray area; thick curves show the stratopause.

Figure 06

Click here to download Rendered Figure: Fig06v2.pdf

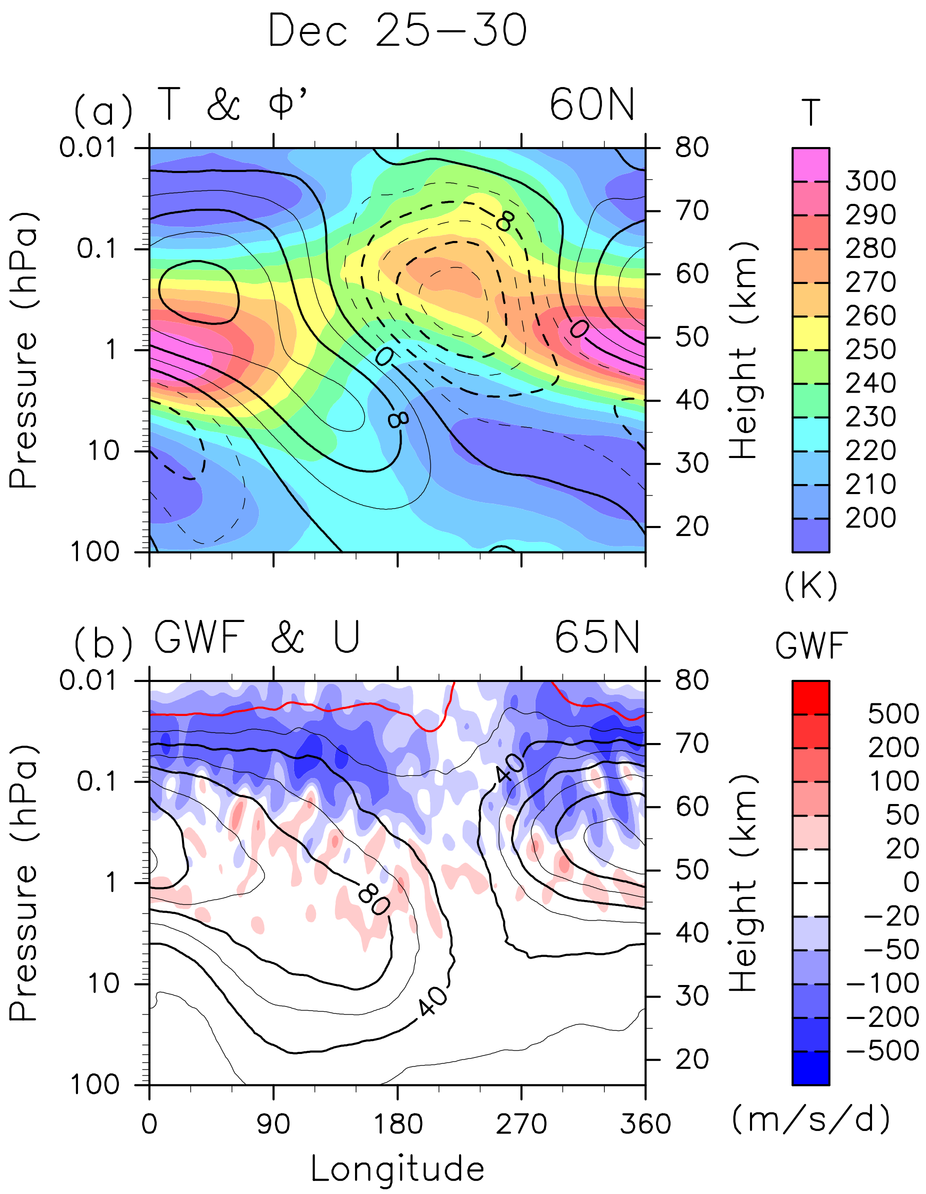

Figure 6. Longitude–height sections of (a) time-mean temperature ($\overline{T}$) (colors) and geopotential anomaly (ϕ') from the zonal mean (contours) at 60°N, and (b) time-mean gravity wave forcing (3DGWF) (colors) and zonal wind ($\overline{u}$) (contours) at 65°N. Contour intervals are (a) 4×10^3 m^2 s^{-2} and (b) 20 m s^{-1}.

Figure 07
Click here to download Rendered Figure: Fig07v2.pdf

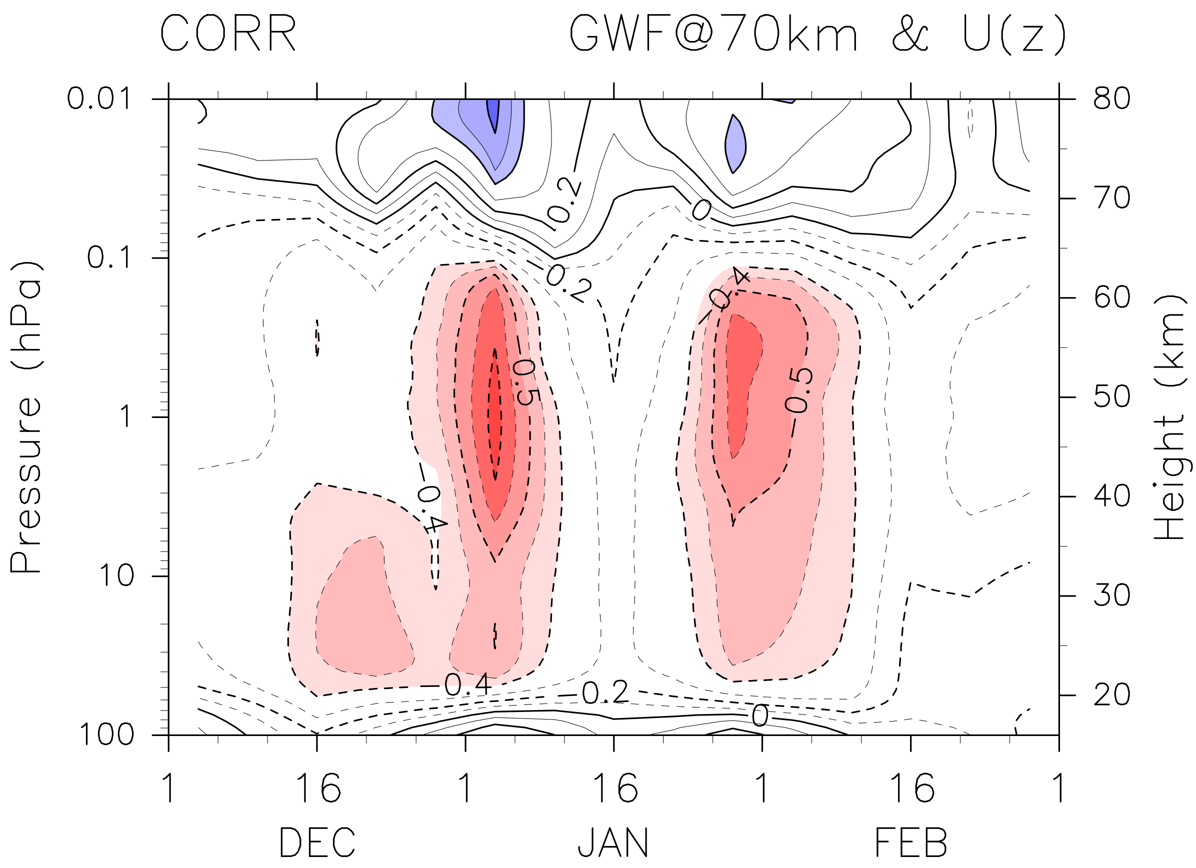

Figure 7. Time–height section of the spatial correlation between gravity wave forcing at 70 km and zonal wind at each level. The vertical axis shows the height of zonal wind.

Figure 08

Click here to download Rendered Figure: Fig08v2.pdf

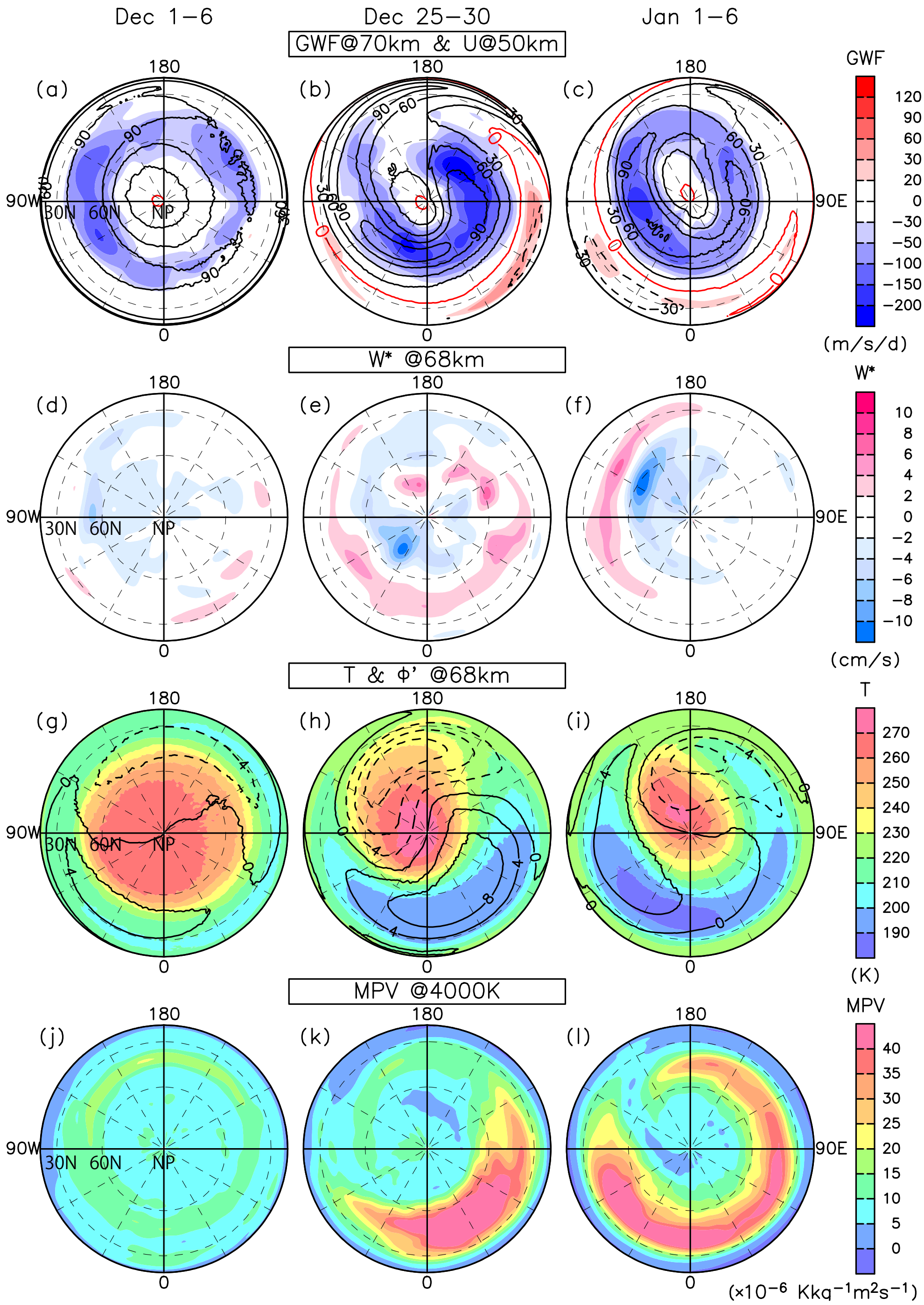

Figure 8. Polar stereo projection maps of time-mean gravity wave forcing (3DGWF) at 70 km (colors) and zonal wind ($\overline{u}$) at 50 km (contours) (a, b, c), residual mean vertical flows ($\overline{w}^*$) at 68 km (colors) (d, e, f), time-mean temperature ($\overline{T}$) (colors) and geopotential anomalies (ϕ') from the zonal mean at 68 km (contours) (g, h, i), time-mean modified potential vorticity (MPV) at 4000 K for (j, k, l), for the N-Period (a, d, g, j), F-Period (b, e, h, k), and M-Period (c, f, i, l). Contour intervals are 30 m s^{-1} (a, b, c) and 4×10^3 $m^2 s^{-2}$ (g, h, i).

Figure 09
Click here to download Rendered Figure: Fig09v2.pdf

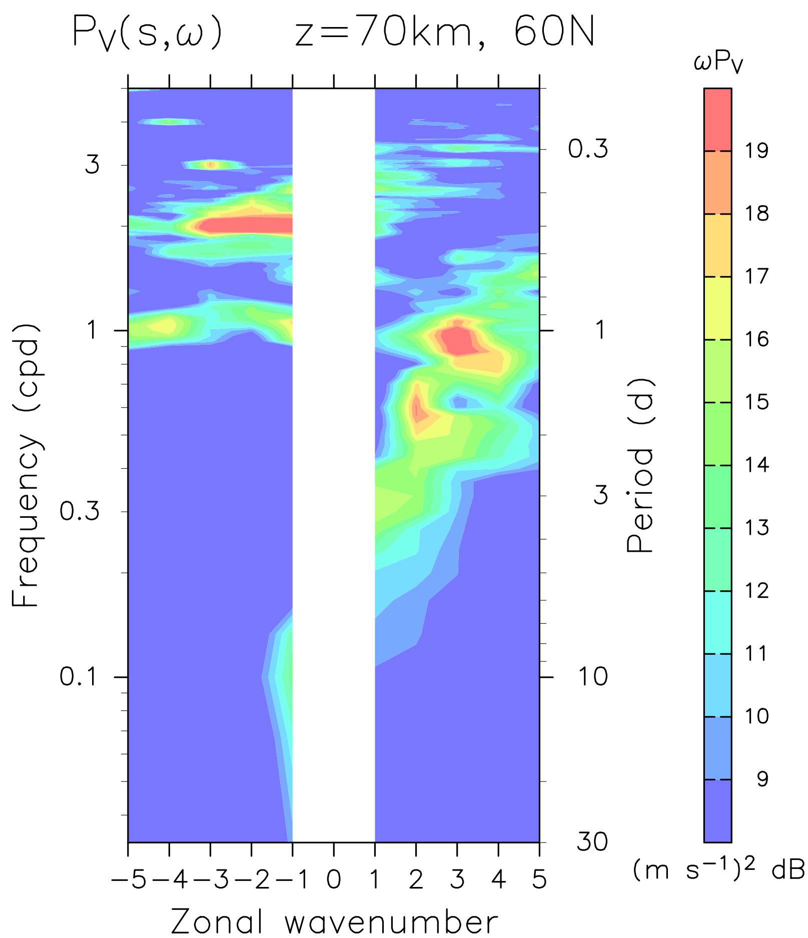

Figure 9. Frequency–zonal wavenumber power spectra of meridional wind fluctuations at 70 km and 60°N for the time period of December 16 to January 15 including F-Period and M-Period. Positive and negative zonal wavenumbers mean eastward and westward phase propagations, respectively.

Figure 10
Click here to download Rendered Figure: Fig10v2.pdf

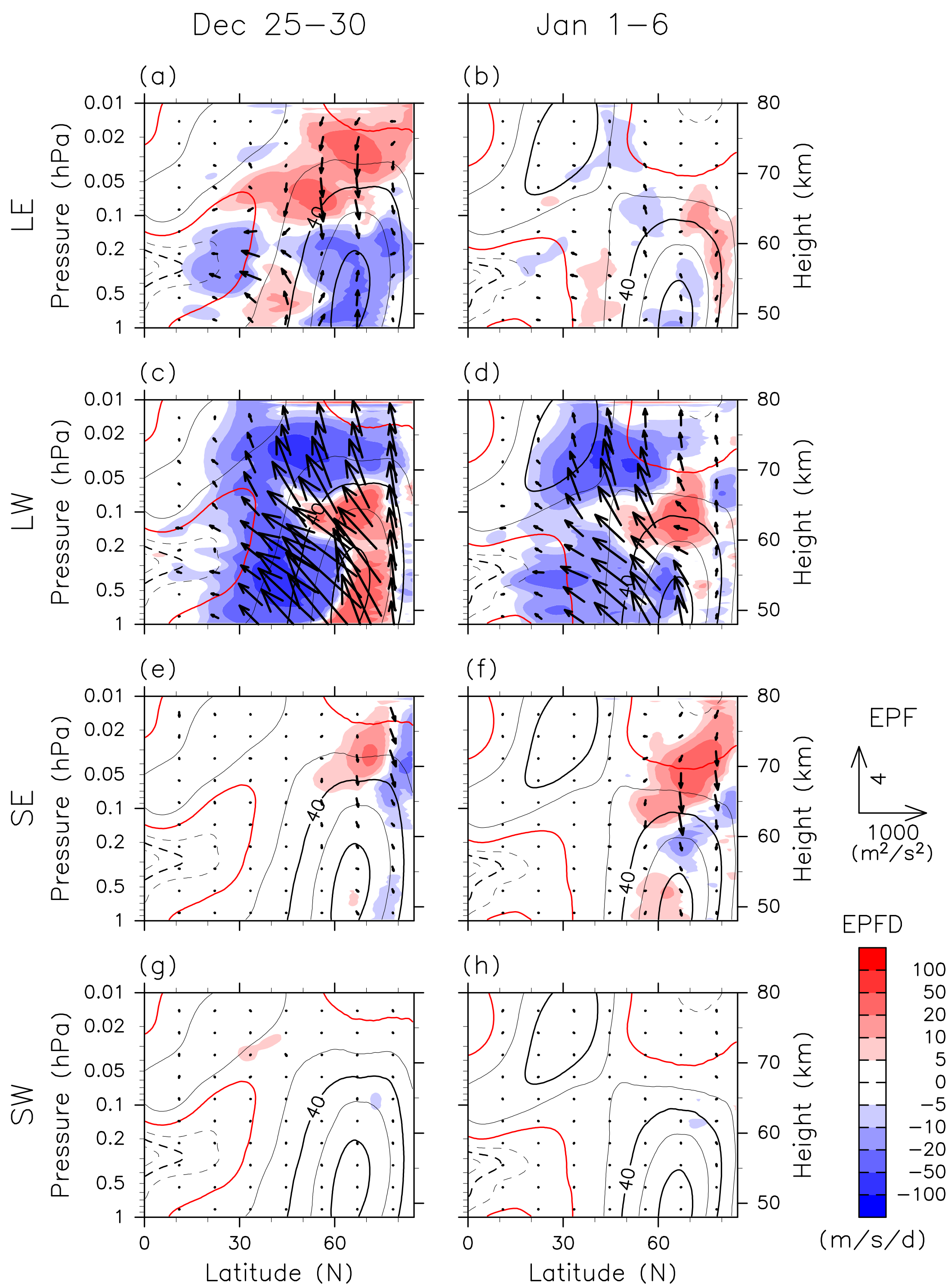

Figure 10. Latitude–height sections of E–P fluxes (vectors), E–P flux divergence (colors) and zonal mean zonal wind ($\overline{u}$) (contours) for long-period eastward planetary waves with $s = 1 - 3$ (PWs) (a and b), long-period westward PWs (c and d), short-period eastward PWs (e and f), and short-period westward PWs (g and h) for the F-Period (a, c, e, g) and M-Period (b, d, f, h). Long and short periods mean the wave periods longer than 6 d and those of 0.6 d to 20 d, respectively. Color scale for the E–P flux divergence is the same as in Fig. 4. Contour interval is 20 m s^{-1}.